QUIET DRONES
Second International e-Symposium
on
UAV/UAS Noise
27th to 30th June 2022

Numerical Investigation of Noise Emissions from a Cargo eVTOL UAV

Michael Schmähl, Technical University of Munich, michael.schmaehl@tum.de
Marcus Gnoth, Phoenix-Wings GmbH, marcus.gnoth@phoenix-wings.de
Mirko Hornung, Technical University of Munich, mirko.hornung@tum.de

Abstract

Urban air mobility (UAM) applications such as cargo electric vertical take-off and landing (eVTOL) unmanned aerial vehicles (UAVs) promise additional transportation capacities for congested urban areas. A major drawback facing UAM operations in future is that the new aerial vehicle movements are bound to lead to additional traffic noise emissions affecting urban areas. Minimum noise designs are therefore essential for UAM aircraft. This paper presents a numerically based computational fluid dynamics (CFD)/Ffowcs Williams-Hawkings (FW-H) model of the noise emissions generated by a cargo eVTOL UAV with separate hover and cruise propellers and focuses on the cruise flight. Installation effects play a predominant role in the noise generation of this highly integrated aerial vehicle configuration. The numerical results of the vehicle's base configuration are validated by inflight noise measurement data. The noise results are split into propeller and airframe components. Alternative tail and propeller configurations are simulated to identify noise reduction potentials that stem from the effects of decreased aerodynamic interaction. It is envisaged that these investigations should form the groundwork for future numerical noise optimizations of the before mentioned base configuration, which explicitly consider the effects of aerodynamic interaction on noise emissions. The noise reduction potentials identified in this study support the idea of parallel rotor and airframe optimization.

1. Introduction

Urban air mobility (UAM) comprises applications such as air taxis or cargo drones and is currently the subject of intensive research within the aerospace community. A study of the societal acceptance of UAM published by the EASA in 2021 reveals that many people have "a positive

initial attitude to UAM" [1, p. 7] but also that noise is one of the main concerns expressed by people in the EU [1, p. 10]. It is therefore clear that research in the field of UAM must also address noise issues.

One of the main focuses of research is on the design of aerial vehicles. A vertical takeoff and landing (eVTOL) configuration is often chosen for UAM aircraft. Many of these configurations are both novel and highly integrated in terms of function, necessitating careful consideration of noise emissions generated throughout the different flight phases. For single rotors with negligible effects stemming from aerodynamic interaction (like it is the case for conventional tractor single propeller configurations), low noise levels can be achieved by reducing blade tip Mach numbers and increasing blade counts (for example, as demonstrated by the acoustic propeller optimization findings published in [2]). However, any noise reductions brought about by these measures come at the cost of aerodynamic efficiency ([3, p. 7]). A theoretical alternative to altering blade number and propeller diameter to achieve noise improvements would be to modify the shape of the blade. However, according to blade element momentum theory (BEMT), there is a distinct chord and twist distribution for which the aerodynamic efficiency of a given propeller is optimal [3, p. 10]. Consequently, any noise improvements achieved through blade shape modifications are at the cost of aerodynamic efficiency.

The overall noise emissions of highly integrated eVTOL configurations can differ significantly from the mere sum of the single propeller's noise contributions (that are regarded as isolated propellers). This is partly due to the effects of the aerodynamic interaction between the different rotors or between the rotor and the airframe, which are, to a certain extent, unavoidable. Another reason is scattering of propeller noise on the airframe [4], which, depending on the size, shape and dominant sound wavelength of the aircraft, leads to interference at far-field observer positions. Optimal noise designs are therefore not necessarily bound to the concept of aerodynamic efficiency versus noise interdependence, in which noise improvements are only possible at the cost of efficiency.

The authors suggest the idea of optimizing the shape parameters of rotors and airframe structures that interact aerodynamically with the rotor in parallel. To assess the potential of such an approach a computational fluid dynamics (CFD)/ Ffowcs Williams-Hawkings (FW-H) model of a pusher propeller cargo eVTOL UAV is set up and validated with in-flight noise measurement data in this paper. The aircraft's noise emissions in cruise flight are significantly impacted by aerodynamic interaction between tail structures and the pusher propeller. In a second step, modifications in the tail/propeller region are then implemented in the model. The aim of the modifications is to influence the aerodynamic interaction in this region while maintaining controllability of the overall aircraft system. Subsequently, the influence of these modifications on noise emissions is assessed.

2. Validation of the CFD/FW-H Noise Model

In this chapter the validation of the CFD/FW-H noise model of the cargo UAV under consideration is presented. It begins with a description of the noise metrics and the noise measurement data which the validation is based upon. Subsequently, the model is introduced and a comparison of simulation and measurement data is given.

2.1 Definition of Noise Metrics

All sound pressure levels (SPL) given in this paper are A-weighted. This reflects the sensitivity of the human ear with respect to the audible frequency spectrum and applies both to instantaneous SPLs, which measure the sound pressure at specific points, and to sound power levels, which are a measure of the overall power of a sound source.

2.2 Noise Measurement Data

The noise measurement data of the cargo UAV considered here was acquired with three ground microphones during an in-flight measurement campaign. In this campaign the aircraft performed a sequence of microphone flyovers and flybys (see Figure 1) such that noise emissions were measured for various aircraft noise emission directions. The noise measurement data were subsequently synchronized with the aircraft log data. The relative velocities between the microphones and the aircraft were then computed and the noise data de-dopplerized on the basis of the relative velocity information. Through this treatment the synchronized noise measurement data is made directedly comparable to the FW-H noise simulation data which is free-field noise without Doppler-frequency shifts. For a more detailed description of the noise data acquisition and processing, refer to [5].

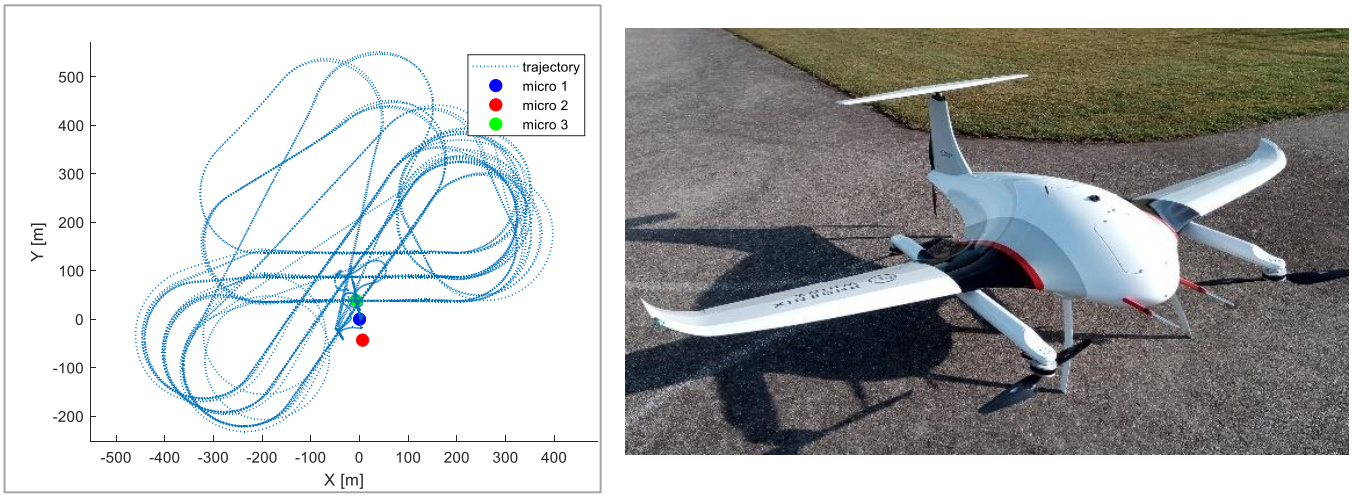

Figure 1: ***Left:*** *flight trajectory and microphone positions;* ***right:*** *cargo eVTOL UAV "Manta Ray" by Phoenix-Wings GmbH*

2.3 Numerical Noise Model

The numerical noise model in this paper adopts a hybrid CFD/FW-H approach. 'Hybrid' in this context means that the approach comprises one step for the numerical CFD solution of the aeroacoustic sound sources, and a separate step for the projection of this source information to the far-field noise receiver points. Both parts of the model are implemented in the starCCM+ CFD software product. For a deeper discussion of the CFD/FW-H noise model setup for UAV-size aircraft, refer to [6].

The meshing in the CFD component of the modelling process is based on CAD models of the airframe and the pusher propeller. Whereas the CAD models on which the closed surface model of the airframe is based were provided by Phoenix-Wings, the propeller was reconstructed from scan data. Potential aeroelastic deformations of the airframe are neglected and the elevator is assumed to be undeflected in the model. The unstructured polyeder mesh consists of *13.0* million cells in the environment domain and *4.6* million cells in the rotating propeller domain. A compressible fluid model is applied which, in combination with a volume mesh not exceeding a maximum cell size of *25 mm* in the area around the propeller and tail, is suitable for resolving the acoustic near field in this source region. An unsteady Reynolds Averaged Navier Stokes (uRANS) approach is applied to model the effect of turbulence in the flow. As turbulent vortices are not explicitly resolved by a uRANS approach, aeroacoustic broadband noise sources are not resolved by the flow simulation. This means that the noise solution is only able to resolve broadband noise to a limited extent.

The acoustic component of the model applies Farassat's formulation 1A of the FW-H integral. All propeller and airframe surfaces are utilized as integration surfaces for the FW-H solver, though relevant aeroacoustic sources are to be expected only in the vicinity of the propeller and tail. This ensures that all relevant source contributions from the airframe are considered, which is

necessary, as the airframe surface data contains pressure fluctuations that originate from sound waves emitted by the propeller. Hence, sound scattering on the airframe is considered by including all airframe surfaces in the FW-H integration surface. The receiver points are located in a sphere with a radius of *30 m* around the center of the propeller.

2.4 Validation of Noise Results

Cruise flight at an airspeed of *25 m/s* and a propeller angular speed of *4150 rpm* is taken as the validation operating point. A comparison of lower sound hemisphere plots for measurement and CFD/FW-H simulation data is given in Figure 2. See the appendix in Figure 17 for a schematic sound hemisphere with an explanatory illustration of the sound emission angles. For the measurement data noise sphere, all measurement samples are converted to a reference distance of *30 m* in order to establish comparability to the simulation data sphere. Measurement and simulation data are in high agreement, both, regarding directivity and magnitude of SPLs. Similarly, the emitted SPL magnitudes exhibit a minimum value of approx. *50 dB(A)* for sound emissions towards the ground (elevation = *-90*°) and a maximum value of approx. *70 dB(A)* for horizontal sideward sound emission (elevation = *0*°, azimuth = ±*90*°).

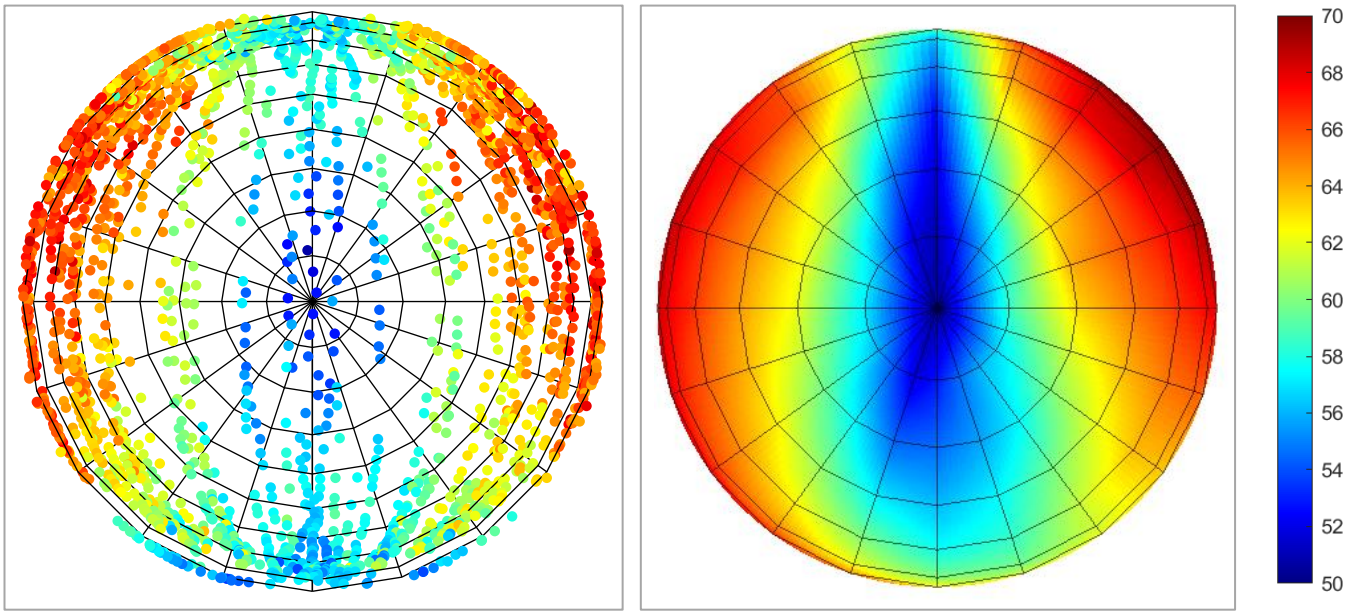

Figure 2: Measurement (left) and simulation (right) over all sound pressure levels (OASPL) [dB(A)], sphere radius: 30 m; grid nodes in simulation hemisphere correspond to receiver points; top: azimuth = 0°, right: azimuth = 90°

Next, the sound spectra of the two noise emission directions are compared. Figure 3 corresponds to noise emission direction towards the ground (elevation = *-90*°) and Figure 4 corresponds to an emission direction inside the propeller plane (elevation = *-30*, azimuth = *90*°) which lies within one of the two noise lobes. Both plots show the blade passing frequency (BPF) tone, which has a frequency of *138.3 Hz*, and a number of BPF harmonics appearing as peaks in the SPL curve.

For noise emission towards the ground, the simulation data is in line with the measurement data, with the BPF showing the highest peak. Compared with the neighboring peaks, the harmonic peaks exhibit smaller SPLs for *n = 3, 9, 14* and higher ones for *n = 6, 11* (peak frequencies described by n*BPF). For sideward noise emissions, the simulation data peaks are in good agreement for *n = 1* to *n = 7*. Concordantly, the peak values are located between *n = 5* and *n = 12*. For frequency peaks higher than *n = 7*, the simulation data over pronounces the SPL peaks. In summary, measurement and simulation spectra are in fair agreement in both emission directions in terms of harmonic tones.

For broadband noise, however, the situation is different. For both emission directions, the CFD/FW-H simulation data does not follow the trend of the broadband noise component in the measurement data. There are two main reasons for this discrepancy. First, the significantly higher broadband in the measurement data for low frequencies can be attributed to background noise, which is not covered by the simulation data. Second, the CFD/FW-H simulation in this study does not explicitly resolve turbulence, and broadband noise can therefore only be resolved to a limited extent.

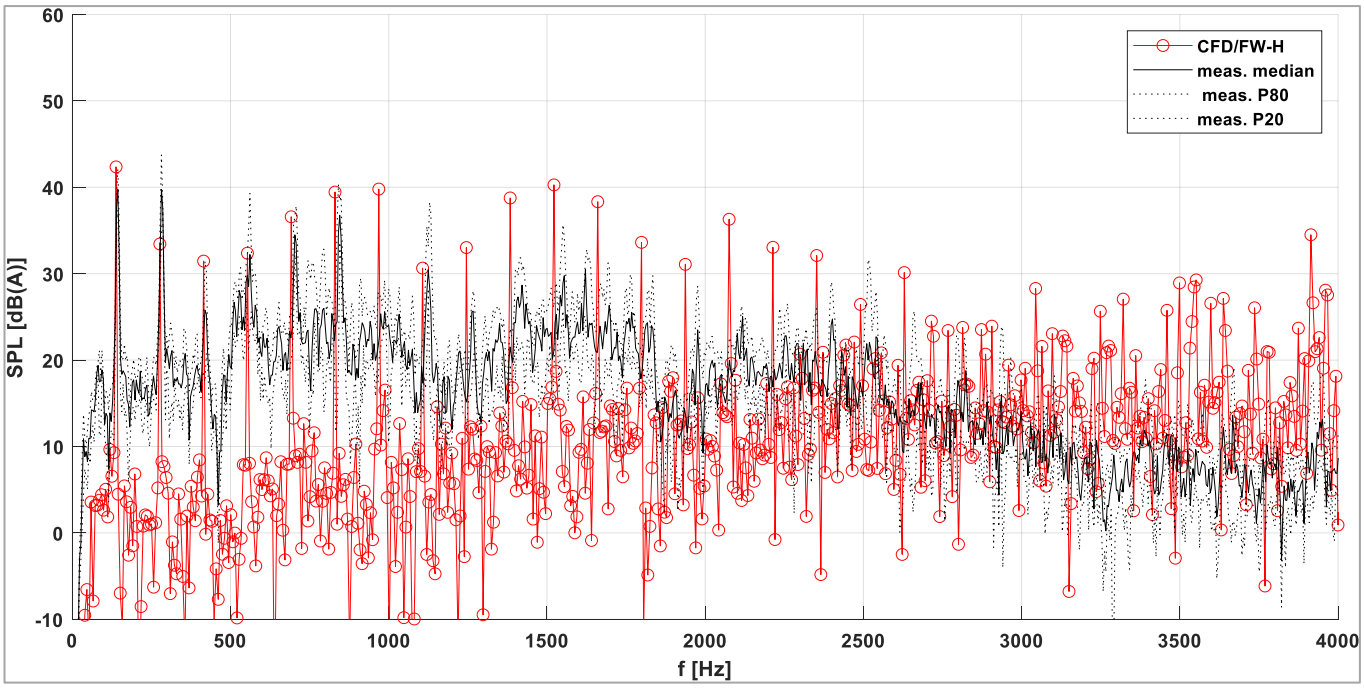

Figure 3: SPL spectrum; noise emission direction: elevation = -90°; median, 20% and 80% percentile curve for measurement data displayed

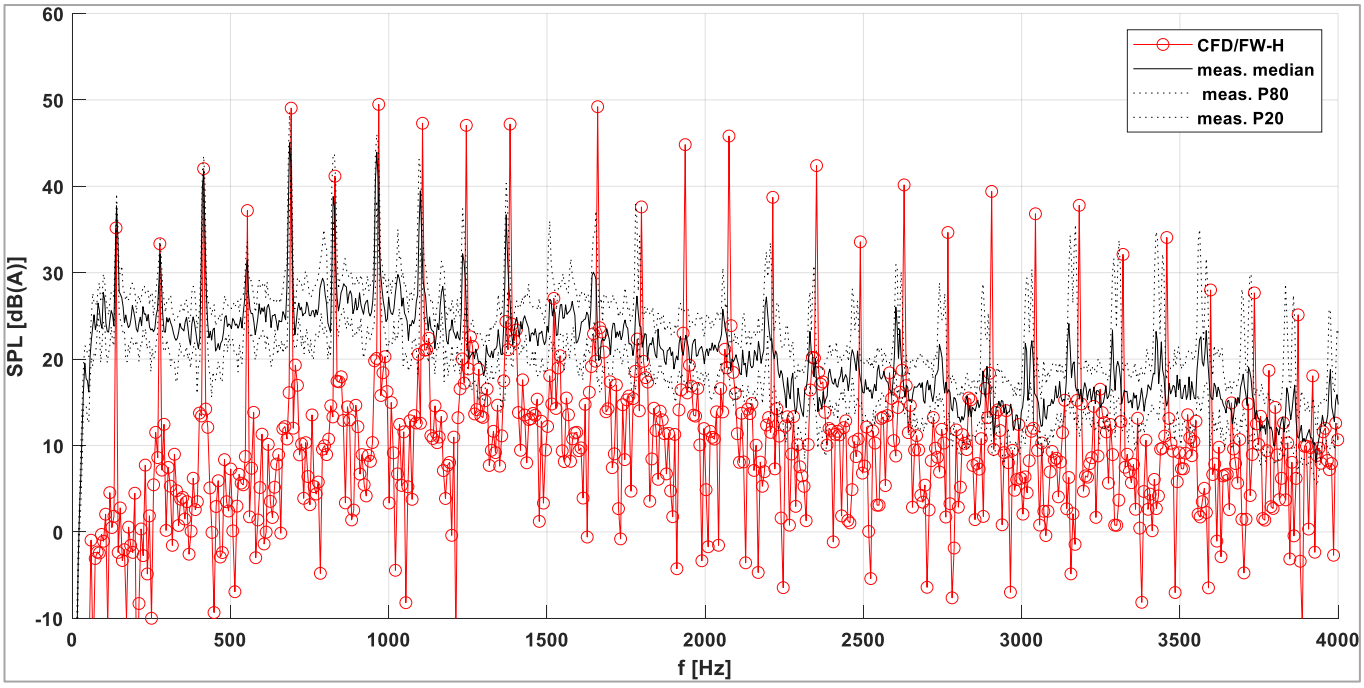

Figure 4: SPL spectrum; noise emission direction: elevation = -30°, azimuth = 90°; median, 20% and 80% percentile curve for measurement data displayed

One way of determining the extent to which the different FW-H surface regions contribute to the overall noise is to split the latter into components corresponding to the various FW-H surfaces.

Figure 5 displays the noise hemisphere, divided into the propeller, the airframe, and the sum of both. Unlike Figure 2, the color scale here is adjusted to give low SPL values a higher visibility. The propeller hemisphere is symmetric with the propeller's rotational axis, which is in accordance with theory [7]. The SPL maxima at azimuth *0*° and *180*° can be attributed to interaction noise. The airframe hemisphere exhibits a clear dipole characteristic, with a minimum in the x, z plane. A comparison of the two components with the hemisphere of both components reveals that the contribution of the airframe to the overall sound emission clearly dominates for most emission directions. Only in the x, z-plane, where the airframe component is at its minimum, does the propeller component contribute significantly to the overall sound emissions.

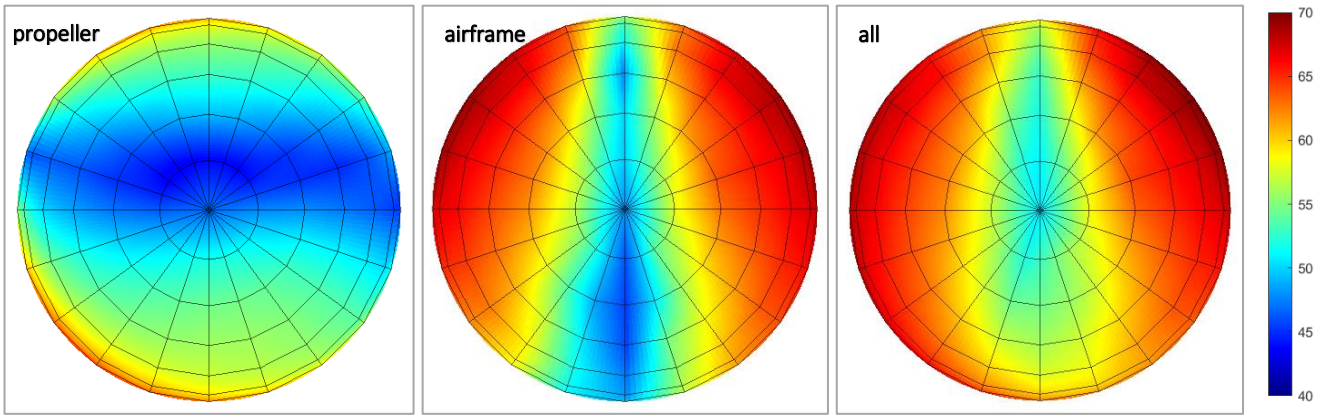

*Figure 5: Simulation data noise hemispheres in [dB(A)]; **left**: propeller only, **center**: airframe only; **right**: all surfaces used for FW-H integration; top: azimuth = 0°, right: azimuth = 90°*

3. Evaluation of Design Modifications

This chapter presents three tail design modifications, the goal of which is to influence the aerodynamic interaction between the airframe and propeller and in turn impact the noise emissions of the overall UAV system. These modifications are implemented in the base CFD/FW-H model and evaluated. This is followed by the CFD/FW-H results, which show the effects of the modifications on aerodynamic interactions and the aeroacoustic noise generation.

3.1 Conception of Design Modifications

Figure 6 and Figure 7 below show all the design modifications. In modification M1, the axial distance between the propeller and tail has been increased by *6 cm*. This increases the absolute tail/propeller distance from approx. *2 cm* to approx. *8 cm*. The aim is to reduce the interaction between the horizontal stabilizer and the propeller by increasing the distance between the two components. In modification M2, the T-tail is replaced by a conceptual V-tail which consists of two NACA0012 profiles. In order to maintain the function of the base tail, the wetted area of the V-tail remains constant in relation to the base tail [8]. Finally, in modification M3, the same profiles as in M2 are rearranged to form an inverse V-tail, which is connected to the hover booms. The design intention of modifications M2 and M3 is to influence the aerodynamic interactions between the tail and propeller by varying the tail type but without to vary the axial positions of the tail surfaces. Essentially, M2 and M3 affect whether or not the tail wakes flow across the propeller disk and, if so, at which propeller disk position the tail wakes interact with the propeller. However, in contrast to M1, they do not significantly affect the strength of the wakes, as the distance between the tail and propeller is kept constant in relation to the base configuration.

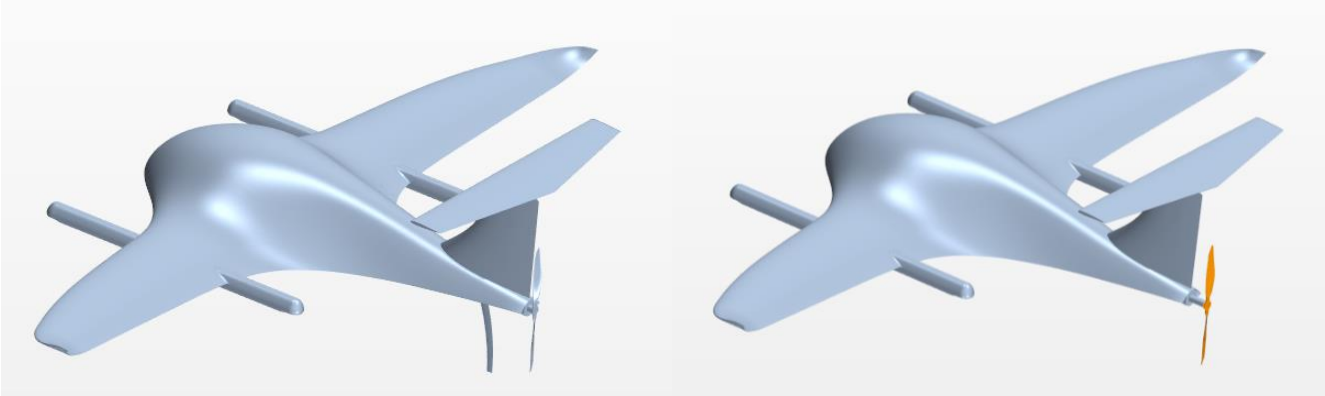

*Figure 6: **Left**: base design; **right**: pusher distance axis distance increased by 6 cm (M1)*

*Figure 7: **Left**: V-tail (M2); **right**: inverted V-tail (M3)*

3.2 Numerical Evaluation of Tail Modifications

Taking a hybrid CFD/FW-H approach, noise predictions are based on the aerodynamic results obtained with the CFD solution. Hence, the evaluation of the tail modifications begins with an assessment of the CFD results and then continues with the FW-H results.

3.2.1 Aerodynamic Results

The extent of the aerodynamic interaction between the flow around the airframe and the propeller tends to be high in pusher propeller configurations. In particular, wakes are present in the flow downstream airframe structures that disturb the propeller inflow. Figure 8 and Figure 9 display the velocity magnitude in a section plane located in the middle between the tail and the propeller, relative to the base configuration, for all four investigated cases. Common to the base configuration and all three modifications is that they show a pronounced horizontal wake due to wing downwash and a comparatively weak vertical wake structure due to the rear landing gear leg. The third wake structure, which leads to the most pronounced velocity deficits compared to the mean flow, is the one caused by the tail. As M1 does not affect the tail, the tail wake of M1 is identical to that of the base. For M3, the propeller does not directly interact with the tail wake. As the inverted V-tail surfaces are located above the propeller, the tail wakes do not flow across the propeller disk.

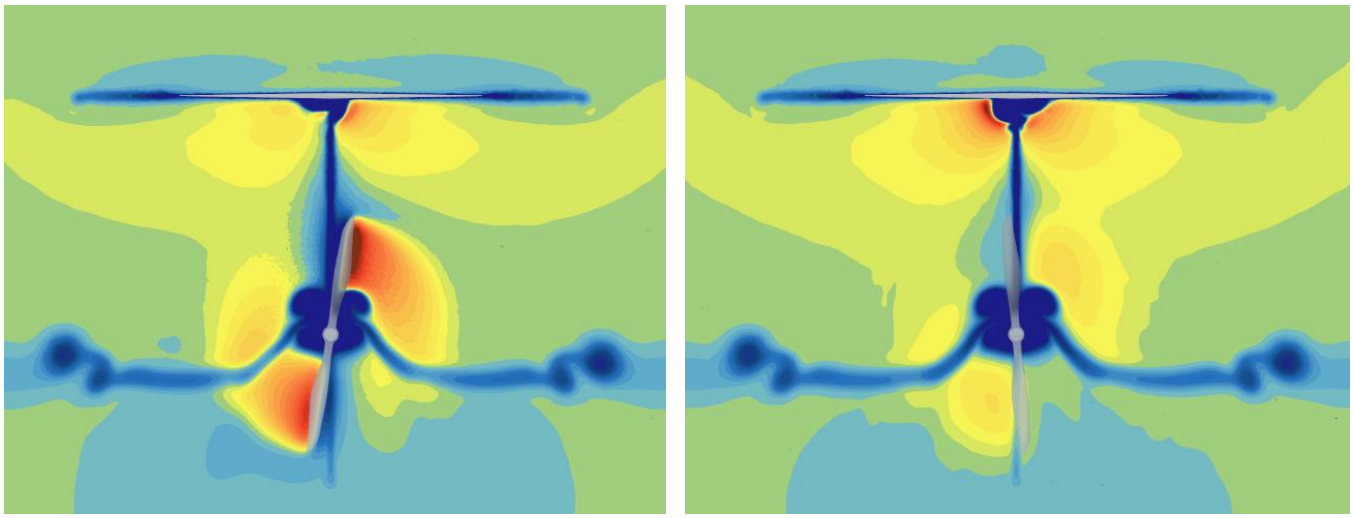

Figure 8: Velocity magnitude on section between tail and propeller; red: 30 m/s and above, blue: 20 m/s and below; ***left:*** *base configuration,* ***right:*** *M1*

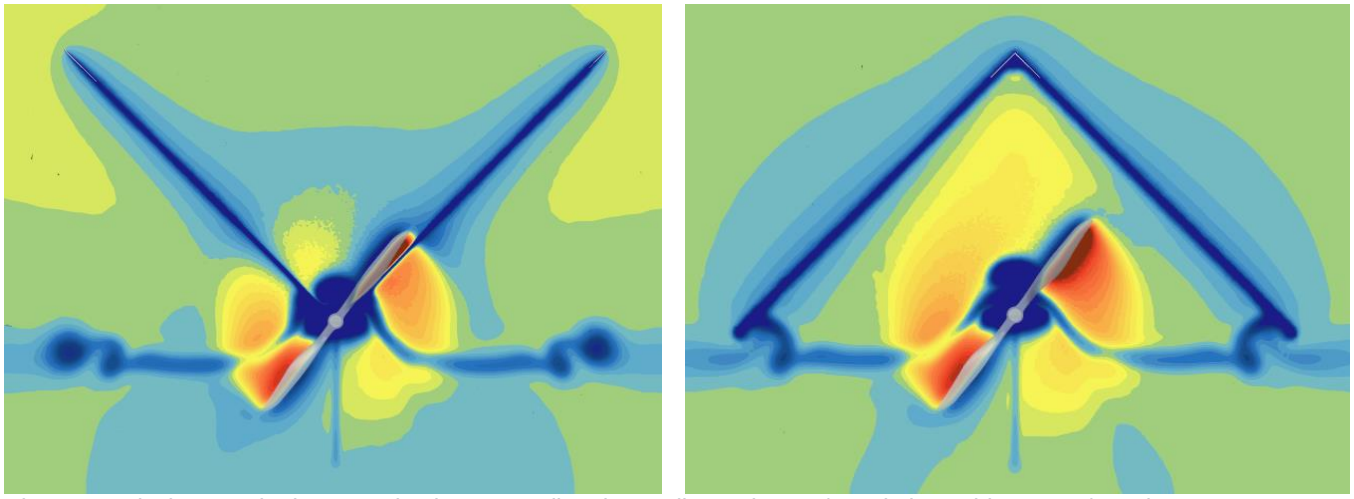

Figure 9: Velocity magnitude on section between tail and propeller; red: 30 m/s and above, blue: 20 m/s and below; ***left:*** *M2****, right:*** *M3*

The aforementioned aerodynamic interaction leads to variations in the velocity and angle of attack of the propeller inflow that affect the propeller thrust. Figure 10 (left) displays the thrust curves of all four simulated cases for one propeller rotation. At *t=0 s,* the two-blade propeller is aligned with the vertical axis. The corresponding FW-H sound pressure result for a receiver point located *30 m* downstream on the propeller axis is displayed on the right-hand side of Figure 10. The time shift between the two diagrams is *0.0889 s,* which equals the sound propagation time for a distance of *30 m*. The effect of the wing and landing gear wakes, which are identical in all cases, is most easily recognizable in the thrust curve of M3, but is present in the other curves as well. While the wing wakes lead to two close peaks, which occur twice per rotation, the landing gear wake leads to thrust peaks that occur right in the middle and at the end of each propeller rotation. For the base configuration and for M1 and M2, the interaction of the propeller with the tail wake adds further peaks to the thrust curve. Since, for a two-blade propeller, the interaction with the vertical stabilizer of the base tail coincides exactly with the one with the landing gear, the tail wake peak of the base configuration is apparently further amplified in relation to the V-tail. The sound pressure diagram on the right of Figure 10 shows that all thrust peaks at emission time coincide with the sound pressure pulses at the respective sound immission times. The strongest sound pressure pulses are caused by the interactions with the tail wakes. It is because of the coincidence of the tail and landing gear interaction in the base configuration that the two tail wake sound pressure pulses of the base configuration are stronger in magnitude than the respective four pulses of M2.

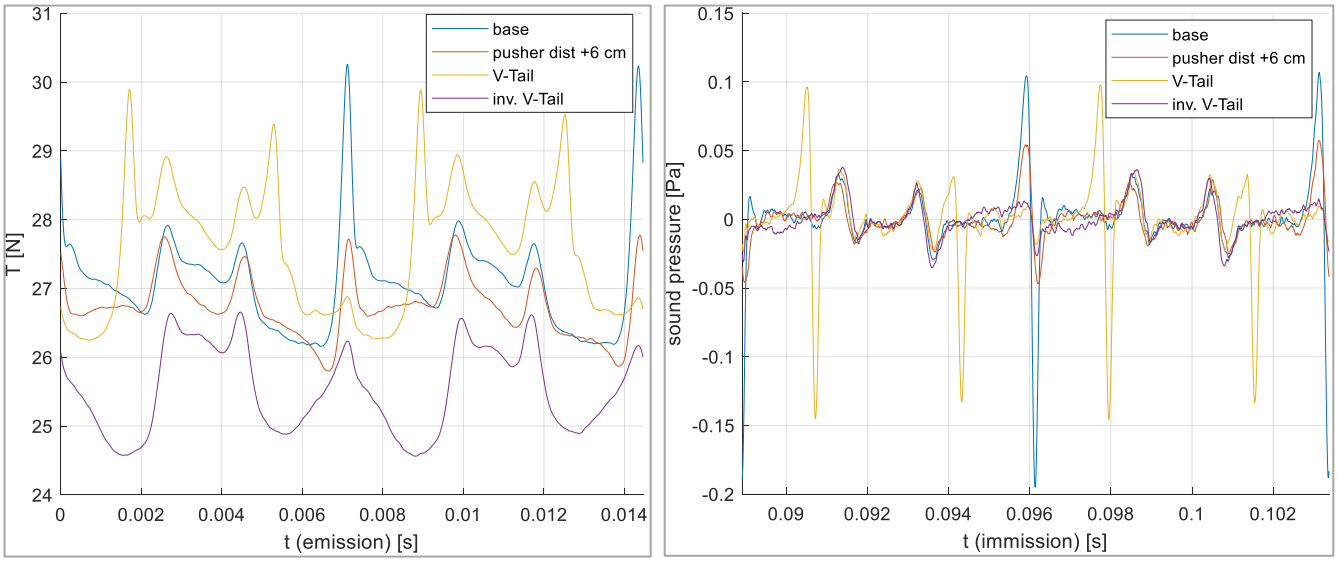

*Figure 10: **Left**: propeller thrust at emission time (for one propeller rotation); **right**: fluctuating component of sound pressure at sound immission time (for one propeller rotation)*

3.2.2 Aeroacoustic Results

This section discusses the lower sound hemisphere representations of the CFD/FW-H noise results obtained for all modifications (Figure 11, Figure 12 and Figure 13) and the corresponding sound power levels (Figure 14). In this analysis, the sound power level of the lower noise hemisphere is chosen as a scalar noise metric. As the noise perception of an observer on the ground is dominated by the lower half of the noise hemisphere, the computation of the sound power level is based on the lower noise hemisphere data.

Figure 11 shows that the axial distance increase in M1 leads to a significant noise reduction compared to the base (see Figure 5), which translates to a sound power level reduction of *11.3 dB(A)*. While the directivity of the M1 propeller noise component in relation to the base is unaffected by this modification, that of the airframe component is significantly changed. Furthermore, the sound power level reduction of the airframe component resulting from M1 (*15.5 dB(A)*) is significantly higher than that of the propeller component (*4.6 dB(A)*). Thus, in contrast to the base configuration, the propeller component dominates the overall sound power level for M1. As in the case of M1, the inverted V-tail of M3 also causes an overall reduction in noise emissions compared to the base configuration. A close examination of the sound power levels and noise hemispheres shows that, as with M1, the inverted V-tail of M3 results in a considerable reduction in the airframe noise component, such that the propeller component dominates the overall aircraft noise emissions of M3. While M1 leads to a reduction in the aerodynamic interaction of the tail wake and the propeller, M3 completely avoids direct interaction of tail wake and propeller. It can be concluded from this comparison that the more aerodynamic interaction is reduced, the less sound power is generated overall by the aircraft.

The V-tail shape in M2 results in a twofold increase in the number of circumferential positions in which a propeller blade interacts with a tail wake. As a consequence, the sound power level of the lower hemisphere increases by *2.0 dB(A)*, due to the increased interaction of the V-tail. As with all other modifications, the directivity of the propeller noise contribution remains similar to the base, while that of the airframe changes significantly.

No significant destructive sound interference effects are found in any of the four simulated cases. In none of the cases is the overall sound emission from the aircraft reduced in relation to the sound emission of the dominant component (propeller or airframe).

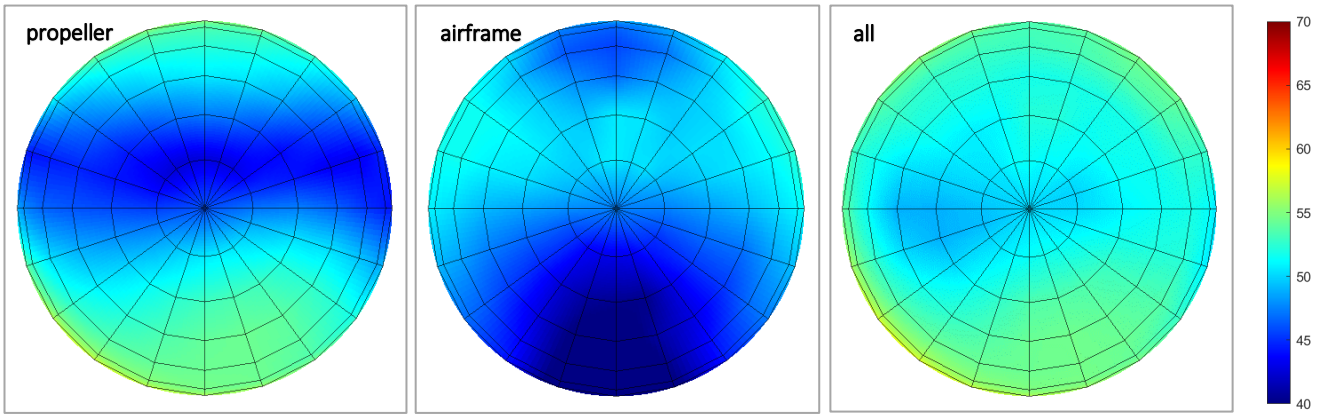

*Figure 11: M1 noise hemispheres in [dB(A)]; **left**: propeller only, **center**: airframe only; **right**: all surfaces used as FW-H integration surfaces; top: azimuth = 0°, right: azimuth = 90°*

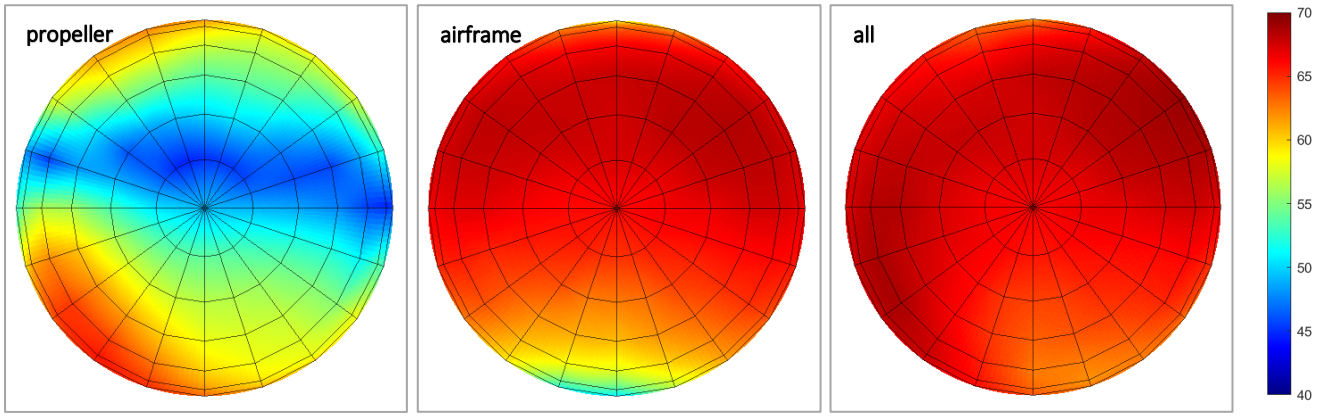

*Figure 12: M2 noise hemispheres in [dB(A)]; **left**: propeller only, **center**: airframe only; **right**: all surfaces used as FW-H integration surfaces; top: azimuth = 0°, right: azimuth = 90°*

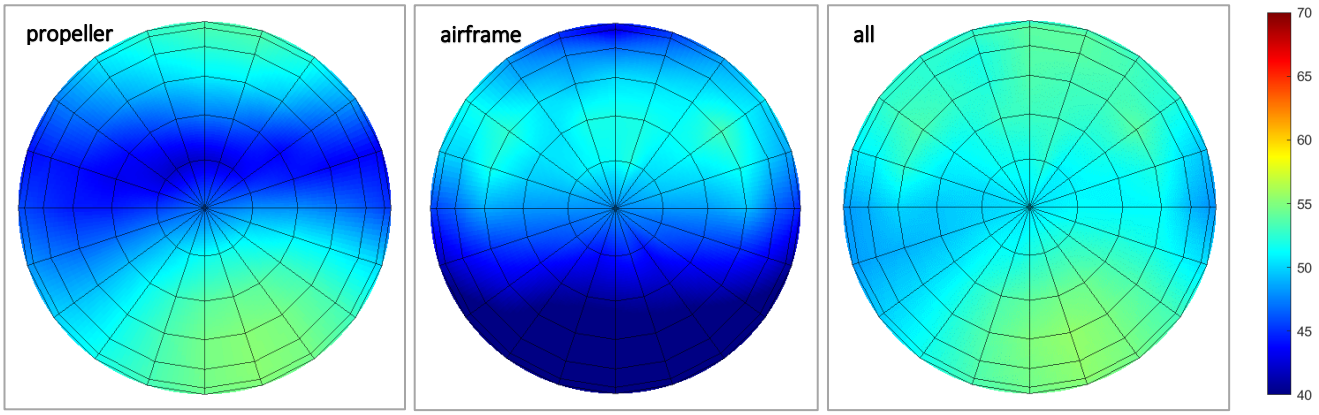

*Figure 13: M3 noise hemispheres in [dB(A)]; **left**: propeller only, **center**: airframe only; **right**: all surfaces used as FW-H integration surfaces; top: azimuth = 0°, right: azimuth = 90°*

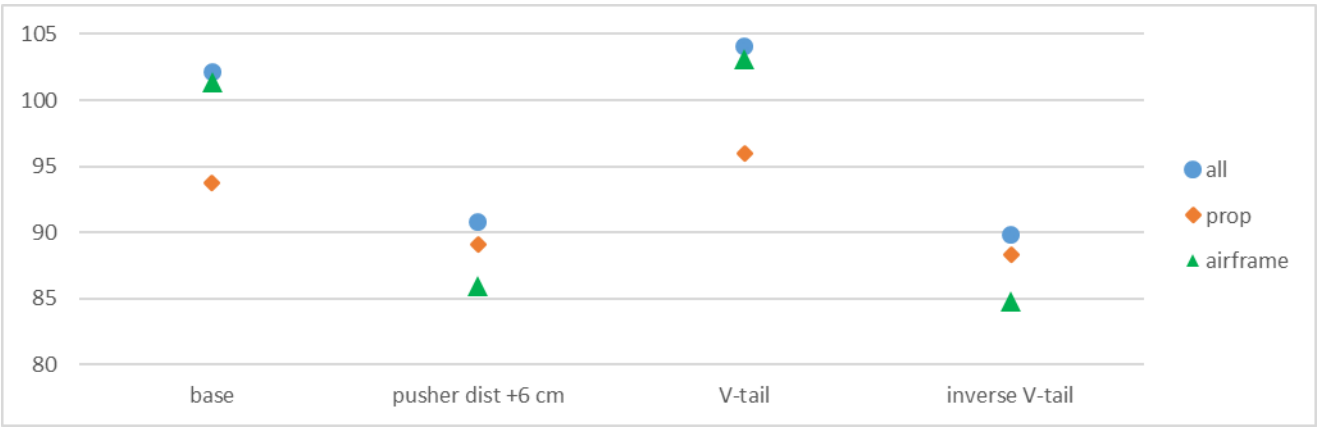

Figure 14: Sound power levels in [dB(A)] for lower hemispheres and UAV variants (base + modifications), divided into contributing surfaces

3.2.3 Airframe Noise

The interaction noise generation mechanism affecting the propeller noise component was considered in section 3.2.1, and this section now discusses the aeroacoustic source mechanism of the airframe component. The base configuration airframe noise component (see Figure 5) exhibits a dipole characteristic, with its plane of symmetry being identical to the orientation of the vertical stabilizer. This observation suggests that the airframe noise is due to fluctuating forces that act on the tail surfaces which are caused by the rotating propeller. Curle's formulation of Lighthill's acoustic analogy can be used to predict the noise emitted from stationary surfaces in an aeroacoustic source region (see [9], [10] and [11]). It is therefore suitable for calculating noise originating from the above source mechanism. If the observer is located in the far-field and the sound source is acoustically compact, the term of the Curle integral that considers fluctuating forces as sound sources can be simplified to:

$$(1) \qquad p'(\vec{x},t) \approx -\frac{1}{4\pi c_0^2 |\vec{x}|} \cdot \frac{x_i}{|\vec{x}|} \cdot \frac{\partial}{\partial t} F_i \left(t - \frac{|\vec{x}|}{c_0} \right)$$

where p' is the sound pressure fluctuation, c_0 is the speed of sound, $|\vec{x}|$ is the point source to observer vector, and F_i is the force vector (where the index i represents Cartesian spatial directions). Acoustic compactness means that the sound wavelength is significantly larger than the source dimension. This assumption is justified for harmonic noise radiating from the tail surfaces, because the BPF wavelength, which is *2.43 m,* is one order of magnitude greater than the chord lengths of the tail surface. Consequently, each of the two tail surfaces in both the base configuration and M2 can be reduced to a point source model according to (1), whose strength is proportional to the time derivative of the respective fluctuating aerodynamic forces. The results of (1) are displayed in the propeller plane in Figure 15. In the base configuration, the vertical stabilizer dipole is significantly stronger than the horizontal one, which is the root cause of the pronounced dipole characteristic in the base configuration. In M2, the dipoles of the two V-tail surfaces superposition in such a way that the dipole directivity pattern cancels out. The full FW-H noise results agree well with the results obtained from (1), which validates this Curle-based tail noise model.

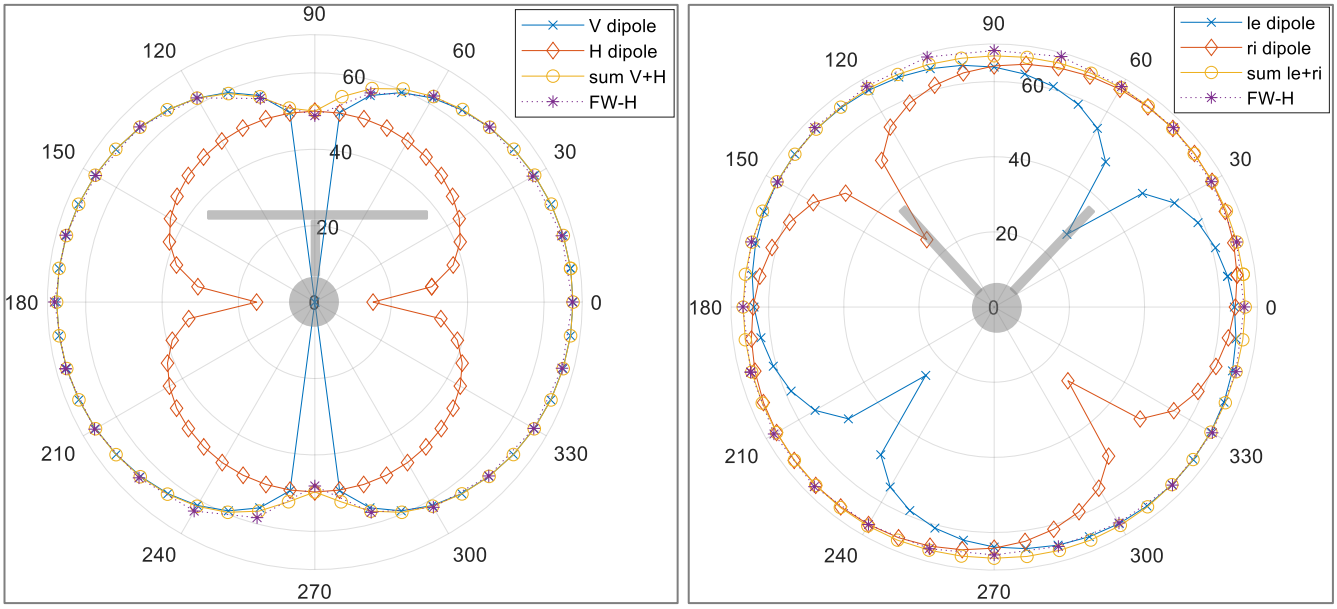

Figure 15: Polar diagrams in [dB(A)] in propeller plane; ***left****: base configuration,* ***right****: V-tail (M2)*

3.2.4 Propeller Performance

Figure 16 shows a plot of the sound power levels over aerodynamic propeller performance for all four cases. The four data points exhibit a basic sound power level versus efficiency correlation. All cases with higher aerodynamic efficiency also have a higher sound power level than the other cases. This behavior is similar to the noise-efficiency correlation stated for isolated propellers in [3], according to which noise reductions are only possible at the cost of aerodynamic efficiency. Although the correlation does not necessarily hold if noise emissions are dominated by interaction effects, none of the three tail region modifications investigated in this paper manages to reduce noise without decreasing aerodynamic efficiency, and vice versa.

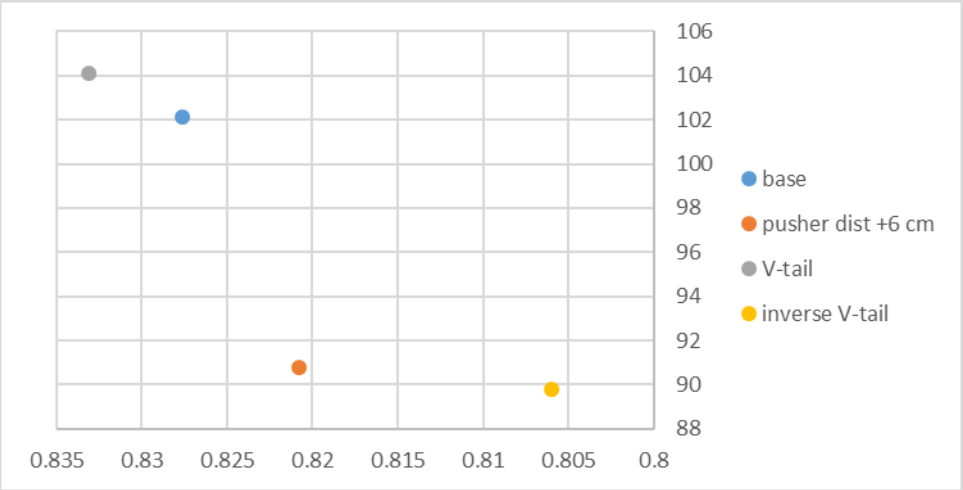

Figure 16: Sound power level [dB(A)] over aerodynamic efficiency [-]

4. Conclusion and Outlook

This paper assesses design modifications in the tail region of an integrated pusher propeller cargo eVTOL UAV. The purpose of the study is to identify noise optimization potentials for propeller-driven UAVs. First, a CFD/FW-H noise model of a cargo UAV is created and validated using in-flight noise measurement data. The lower noise hemispheres and the sound spectra comparison for two representative noise emission directions shows agreement between the measurement and simulation data. Second, design alternatives affecting the main aeroacoustic source region are suggested; these are implemented in the CFD/FW-H model and assessed numerically. The results of this simulation campaign show that noise generation is reduced by decreasing the aerodynamic interaction between the tail wakes and the propeller.

All in all, this study has identified significant noise reduction potential, supporting the idea of simultaneous optimization of the propeller and airframe. Potential for acoustic optimization can be particularly found in highly integrated configurations in which aerodynamic interactions are unavoidable, as is the case with the UAV considered in this paper. The work presented in this paper only considers airframe modifications but elaborate modifications of both, airframe and propeller, can lead to further reductions in noise.

This study employs a high-fidelity CFD model to obtain a reliable data base with which to assess the acoustic effects of the design modifications in the tail region. A major drawback of this approach is the high computational cost. Future design optimization necessitates a high number of model evaluation. Consequently, a computationally more efficient medium-fidelity CFD approach that is sufficiently accurate to resolve the effects of aerodynamic interaction will be required in future optimizations. To achieve this, the authors suggest using an unsteady BEMT in future work.

5. Appendix

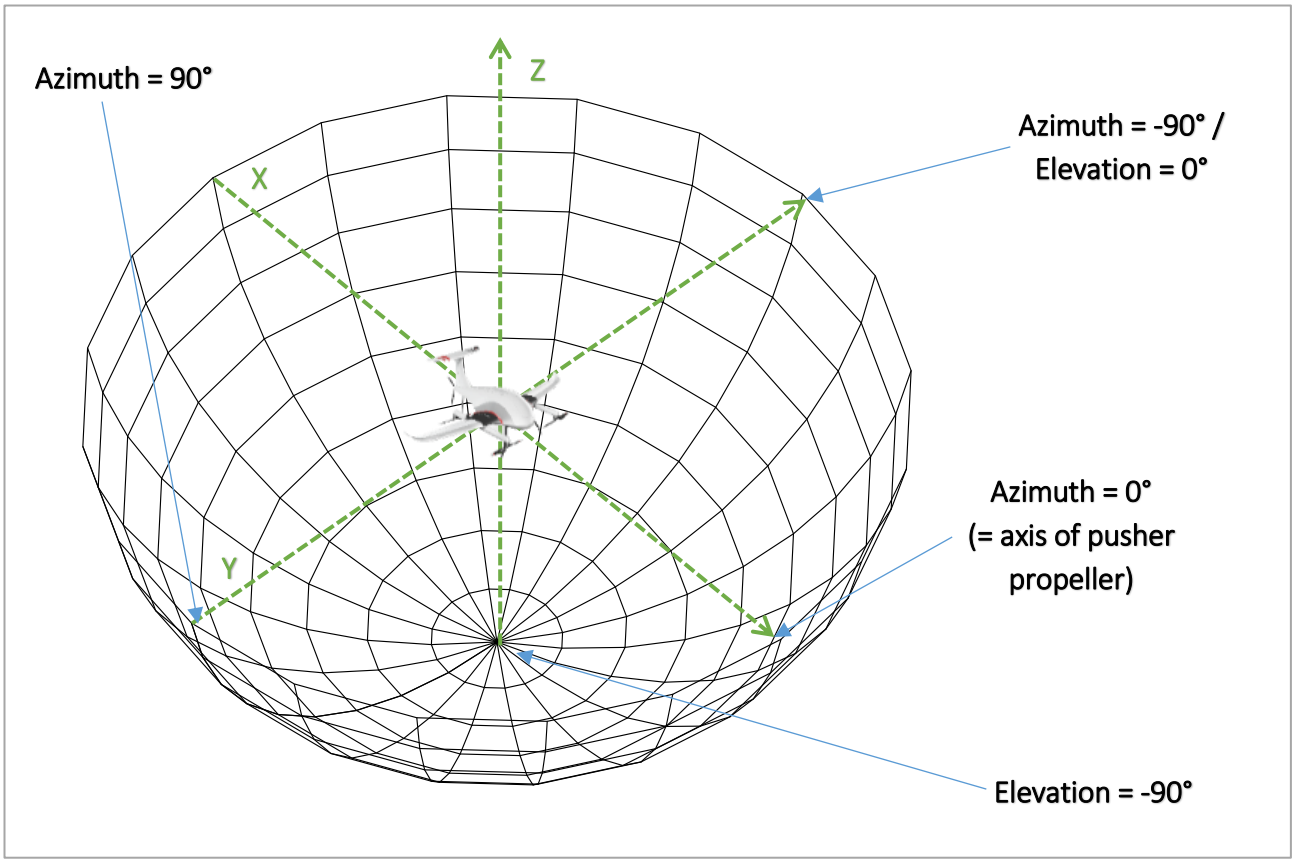

Figure 17: Lower sound hemisphere sketch showing sound emission directions

References

[1] EASA, "www.easa.europa.eu," 2021. [Online]. Available: https://www.easa.europa.eu/sites/default/files/dfu/uam-full-report.pdf. [Accessed 4th of November 2021].

[2] S. Speck, J. Pfefferkorn, K. Kicker and M. Hornung, "Methoden zur Bewertung und Minimierung der Signatur von unbemannten Flugzeugen," in *Deutscher Luft- und Raumfahrtkongress*, Stuttgart, 2013.

[3] A. M. Stoll, "Design of Quiet UAV Propellers," Stanford University, Stanford, CA, 2012.

[4] J. Yin and A. Stürmer, "Coupled uRANS and FW-H Analysis of Installed Pusher Propeller Aircraft Configurations," Miami, Florida, 2009.

[5] M. Schmähl, C. Rieger, S. Speck and M. Hornung, "Semi-empiric noise modeling of a Cargo eVTOL UAV by means of system identification from flight noise measurement data," *CEAS Aeronautical Journal,* pp. 85-96, 01 01 2022.

[6] M. Schmähl, S. Speck and M. Hornung, "Numeric Modeling of the Noise Emission of a Pusher Propeller UAV Configuration," in *AIAA SCITECH 2022 Forum*, San Diego, CA, 2022.

[7] J. E. Marte and D. W. Kurtz, "A Review of Aerodynamic Noise From Propellers, Rotors, and Lift Fans," NASA, Washington, D.C., 1970.

[8] D. Raymer, Aircraft design: a conceptual approach., American Institute of Aeronautics and Astronautics, Inc., 2012.

[9] M. J. Lighthill, "Lighthill, Michael James. "On sound generated aerodynamically I. General theory.," *Proceedings of the Royal Society of London. Series A. Mathematical and Physical Sciences,* vol. 211, no. 1107, pp. 564-587, 1952.

[10] M. J. Lighhill, "Lighthill, Michael James. "On sound generated aerodynamically II. Turbulence as a source of sound.," *Proceedings of the Royal Society of London. Series A. Mathematical and Physical Sciences,* vol. 222, no. 1148, pp. 1-32, 1954.

[11] N. Curle, "The influence of solid boundaries upon aerodynamic sound.," *Proceedings of the Royal Society of London. Series A. Mathematical and Physical Sciences ,* vol. 231, no. 1187, pp. 505-514, 1955.